Strain Rate Sensitivity, Work Hardening, and Fracture Behavior of an Al-Mg TiO_2 Nanocomposite Prepared by Friction Stir Processing

FARZAD KHODABAKHSHI, ABDOLREZA SIMCHI, AMIRHOSSEIN KOKABI, MARTIN NOSKO, and PETER ŠVEC

Annealed and wrought AA5052 aluminum alloy was subjected to friction stir processing (FSP) without and with 3 vol pct TiO_2 nanoparticles. Microstructural studies by electron backscattered diffraction and transmission electron microscopy showed the formation of an ultra-fine-grained structure with fine distribution of TiO_2 nanoparticles in the metal matrix. Nanometric Al_3Ti and MgO particles were also observed, revealing *in-situ* solid-state reactions between Al and Mg with TiO_2. Tensile testing at different strain rates determined that FSP decreased the strain rate sensitivity and work hardening of annealed Al-Mg alloy without and with TiO_2 nanoparticles, while opposite results were obtained for the wrought alloy. Fractographic studies exhibited that the presence of hard reinforcement particles changed the fracture mode from ductile rupture to ductile-brittle fracture. Notably, the failure mechanism was also altered from shear to tensile rupture as the strain rate increased. Consequently, the fracture surface contained hemispherical equiaxed dimples instead of parabolic ones.

DOI: 10.1007/s11661-014-2330-1

I. INTRODUCTION

ALUMINUM matrix nanocomposites (AMNCs) are an important class of new materials for structural and electrical applications.[1] Particulate-reinforced AMNCs are of particular interest because of their isotropic properties and relatively low-cost fabrication procedure.[2] It is well established that the mechanical properties of AMNCs are controlled by the size and volume fraction of the reinforcements as well as the nature of the matrix-reinforcement interface.[1] Superior mechanical properties can be achieved when fine and stable reinforcements with good interfacial bonding are dispersed uniformly in the matrix,[3,4] which can be achieved *via in-situ* reactions upon processing. Various methods such as mechanical alloying (MA),[5] reactive hot pressing (RHP),[6] reactive squeeze casting (RSC),[7] and combustion synthesis[8] have been used to prepare AMNCs, in which the reinforcement particles are formed *in situ* during processing. When the fabrication process is combined with severe plastic deformation of the metal matrix, the grain structure is also refined yielding another advantage of ultra-fine-grained materials with regard to mechanical properties.[9]

Friction stir processing (FSP) is a relatively new solid-state procedure for the fabrication of AMNCs.[10–17] In this process, a rotating tool pin is plunged into the surface of metallic sheets and traversed along their surface. The friction and plastic deformation imposed by the tool heat and soften the workpiece, while the tool pin promotes intermixing of material in a local region.[18] Severe plastic deformation of the metal matrix promotes mixing and refining of the grain structure and constituent phases, while the local temperature rise facilitates the formation of intermetallic phases such as Al_3Fe, Al_2Cu, Al_3Ni, and Al_3Ti.[10–12,15,17] Consequently, the fine-grained structure and homogeneous distribution of hard particles yield superior mechanical properties.

For instance, Hsu *et al.*[10] and Zhang *et al.*[19] reported a considerable enhancement in elastic modulus and yield strength of Al-Al_3Ti nanocomposites fabricated by reactive FSP of Al-Ti powder mixtures; similarly, Zhang *et al.*[17,20] processed Al-TiO_2 sheets and showed a significant grain refinement together with *in-situ* formation of Al_3Ti and Al_2O_3 phases, which enhanced mechanical strength; studies also were performed on the fabrication of Al-Al_3Ni, Al-Al_3Fe, and Al-Al_2Cu nanocomposites by reactive FSP of Al-Ni,[21] Al-Fe,[12] and Al-Cu.[22] Despite the potential application and advantages of reactive FSP for the fabrication of AMNCs, further investigations are required to determine the microstructure-mechanical property relationship aiming to promote our understanding of the texture development, flow stress behavior, and

FARZAD KHODABAKHSHI, Ph.D. Student, and AMIRHOSSEIN KOKABI, Professor, are with the Department of Materials Science and Engineering, Sharif University of Technology, Azadi Avenue, P.O. Box 11365-9466, 14588 Tehran, Iran. ABDOLREZA SIMCHI, Professor, is with the Department of Materials Science and Engineering and Institute for Nanoscience and Nanotechnology, Sharif University of Technology, P.O.Box 11365-9466, 14588 Tehran, Iran. Contact e-mail: simchi@sharif.edu MARTIN NOSKO, Assistant Professor, is with the Institute of Materials and Machine Mechanics, Slovak Academy of Sciences, Račianska 75, 83102 Bratislava, Slovak Republic. PETER ŠVEC, Professor, is with the Institute of Physics, Slovak Academy of Sciences, Dúbravská cesta 9, 845 11 Bratislava 45, Slovak Republic.

Manuscript submitted December 11, 2013.
Article published online May 17, 2014

fracture mechanisms. Particularly, studies on strain rate sensitivity and work hardening are important for subsequent thermomechanical treatments that make the processed sheets applicable for the fabrication of functional products. The role of pretreatment (annealed or wrought sheets) on the microstructural developments upon FSP and the resulting mechanical properties should also be evaluated, because prestored strain energy can affect the strain rate sensitivity, work hardening, and fracture behavior of the processed samples.

The aim of the present work is to study the microstructural development, texture formation, and fracture behavior of a friction-stir-processed Al-2.2 pct Mg-3 vol pct TiO_2 nanocomposite. Annealed and wrought Al-Mg alloy sheets were used to examine the effects of pretreatment (metallurgical history) on the microstructural development and mechanical properties. Preplaced TiO_2 nanoparticles were used to promote the *in-situ* reaction upon FSP, yielding nanometer-sized Al_3Ti as reinforcement particles. Tensile testing was performed at strain rates ranging from 0.001 to 0.1 s^{-1} to explore the flow stress behavior of the examined materials. It is noteworthy that the strain rate sensitivity and flow behavior of Al-Mg alloys fabricated at different processing conditions were frequently investigated.[23–28]

Superplasticity of Al-Mg alloys is commonly related to grain refinement and increased strain rate sensitivity. However, in friction-stir-processed AMNCs, the presence of hard inclusions should alter the flow behavior and the effect of strain rate on the fracture behavior. Particularly, *in-situ* reactions between the metal matrix and additives (*e.g.*, TiO_2 nanoparticles) during FSP could lead to Mg depletion that affects the flow behavior of the processed sheet upon tensile testing and its fracture behavior.[29] On the other hand, pretreatment of the alloy sheets can influence the flow patterns through the stir zone (SZ) during FSP and, thus, affect microstructural evolution, crystallographic textural development, and plastic deformation, topics that have not been investigated in detail to the authors' best knowledge. This article presents the experimental results on the tensile flow behavior and fracture of Al-2.2 pct Mg alloy reinforced with Al_3Ti and MgO phases processed *via* FSP.

II. EXPERIMENTAL PROCEDURE

A. *Materials*

Wrought AA5052 sheets in H32 heat treatment condition with chemical composition 97.04Al-2.23Mg-0.292Fe-0.163Cr-0.147Si-0.114Mn-0.0077Zn-0.0065Cu (wt pct) were supplied by Arak Aluminum Co. (Arak, Iran). To study the effect of pretreatment, a batch of sheets was subjected to an annealing heat treatment at 500 °C for 2 hours followed by water quenching. Titanium dioxide powder with chemical purity ~99.99 pct and average particle size ~30 nm in the anatase phase was purchased from US Nano Company (Houston, TX).

B. *Friction Stir Processing*

FSP of the annealed and wrought Al-Mg alloys was performed using a cylindrical nonconsumable tool made from H13 steel with specifications summarized in Table I. This tool was heat treated to 48 HRc before use. For the preparation of Al-Mg-TiO_2 nanocomposite, rectangular grooves with dimensions of 210 × 3.5 × 1.2 mm were machined in the middle of annealed and wrought sheets. After cleaning with acetone, the grooves were filled with TiO_2 nanoparticles. To encapsulate the nanoparticles, the grooves were sealed by a prefriction stir treatment with conditions given in Table I. Afterward, four-pass FSP was employed parallel to grooves with 100 pct overlap to obtain a uniform dispersion of nanoparticles through the metal matrix. Figure 1(a) demonstrates the details of the FSP process used in this study.

C. *Microstructure and Texture Evaluations*

The aspects of sample preparation for microstructural studies are shown in Figure 1(b). To prepare cross-sectional specimens for microstructural studies, electric discharge machining was used. After employing the standard metallographic procedure by consecutive SiC abrasive papers (320, 600, 800, 1200, and 2500) and mechanical polishing with diamond solutions (10, 3, and 1 μm), a modified Poulton's chemical solution was used for chemical etching for 5 to 10 seconds. The etchant was composed of 1 mL H_2O/6 mL HNO_3/1 mL HF/12 mL HCl and 25 mL HNO_3/1 g H_2CrO_4/10 mL H_2O solutions.

The microstructure of the SZ, thermomechanically affected zone (TMAZ), heat-affected zone (HAZ), and base metal (BM) was examined using an Olympus (OM) PME3 equipped a digital camera and a CLEMEX-BX51M image analyzer, Germany. A field-emission scanning electron microscope (FESEM, JEOL*)

*JEOL is a trademark of Japan Electron Optics Ltd., Tokyo.

Table I. Tool Specifications and Process Conditions Used to Accomplish FSP

Specifications	Tools						Process		
Parameters	Shoulder Diameter (mm)	Pin Diameter (mm)	Pin Height (mm)	Thread Depth (mm)	Thread Angle (Deg)	Nuting Angle (Deg)	Rotational Velocity (rpm)	Traverse Speed (mm/min)	Number of Pass
Capping pass	12	—	—	—	—	2.5	1125	30	1
Main FSP	18	5	4	0.5	30	2.5	1200	100	4

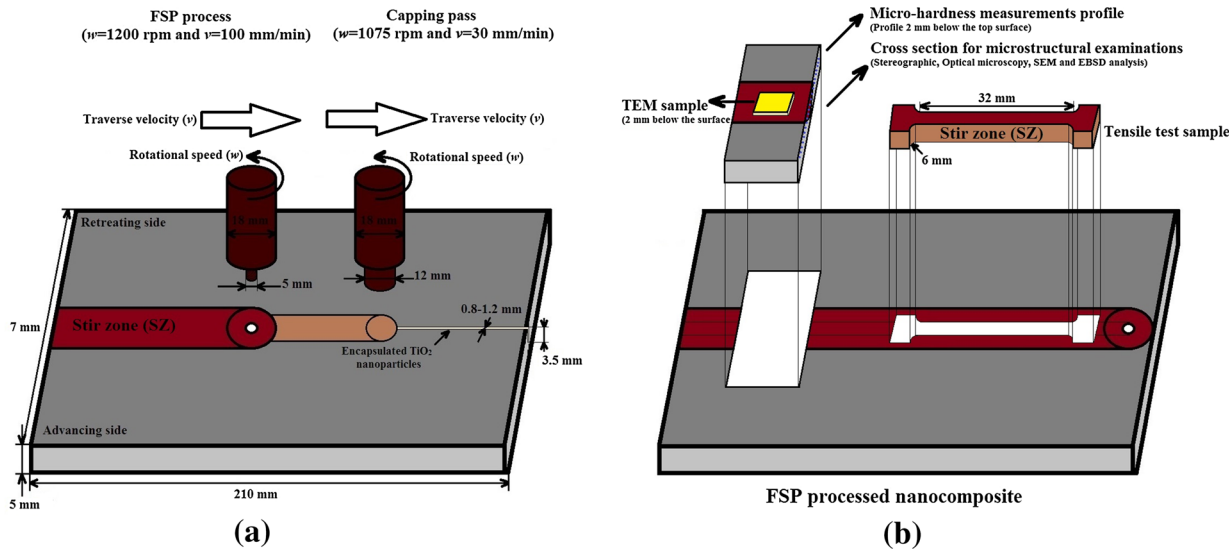

Fig. 1—Schemes show (*a*) FSP process accomplishment and (*b*) sample preparation for microstructural characterization and mechanical testing.

equipped with an electron backscattered diffraction (EBSD) detector was used for studying the grain structure and crystallographic texture of the specimens. Before EBSD studies, metallographic sections were subjected to ion milling (JEOL) to release the surface residual stresses. Grains with misorientation angles in the range of 1.5 to 15 deg were considered low-angle grain boundaries (LAGBs), while boundaries with higher misorientation angles higher were regarded as high-angle grain boundaries (HAGBs). Mechanical polishing and ion milling were used to prepare thin samples (~50 nm) for transmission electron microscopy (TEM). Examinations were performed by a JEOL 2000FX transmission electron microscope and a CM300 Philips high-resolution transmission electron microscope (HRTEM CM300, Philips, Amsterdam, Netherlands) operated at 200 and 300 kV, respectively.

D. *Mechanical Characterizations*

To determine the hardness profile along different zones, a Vickers microindenter (Böhler-Uddeholm, Düsseldorf, Germany) at a load of 0.3 kg and dwell time of 15 seconds was used. The measurements were carried out along the cross section about 2 mm below the top surface (Figure 1(b)). To evaluate the mechanical properties of the processed specimens, tensile testing at strain rates of 0.001, 0.01, and 0.1 s^{-1} was performed. The range of the applied strain rate was in the quasi-static loading condition. A uniaxial tensile test at ambient temperature was performed on samples with a gage length of 32 mm machined from the SZ along the FSP direction in accordance with the ASTM E8 standard.[30] These tensile samples were prepared from the middle of the SZ with a cross-sectional area of 6 × 4 mm^2, as schematically shown in Figure 1(b). An INSTRON** universal tensile loading machine with a load cell of 10-kN capacity and frame stiffness of 100 kN/mm was used. All tests were performed under the strain rate control condition. An HT self-supporting axial extensometer of series 3448 (Epsilon Tech, WY, USA) was used during tensile loading to monitor and record the load displacement at the gage length. For each condition, tensile testing was repeated 3 times and the mean values were reported. The fracture surface of the examined samples was studied by FESEM.

**INSTRON is a trademark of Illinois Tool Works Inc. (ITW), Glenview, IL.

III. RESULTS

A. *Microstructural Characterization*

Cross-sectional images of the Al-Mg alloy and Al-Mg-TiO_2 nanocomposite prepared from FSP of the annealed and wrought sheets are presented in Figures 2, 3, and 4. The mean values of the grain size in different zones (BM, HAZ, TMAZ, and SZ) are reported in Table II. Microstructural studies indicated that the size of SZ in the wrought samples was larger than that of the annealed specimens (Figure 2). A wider onion ring structure was also seen in the wrought samples while the distribution of TiO_2 nanoparticles was poorer (*i.e.*, coarse powder agglomerates were observed). At a higher magnification, refinement of the grain structure of the

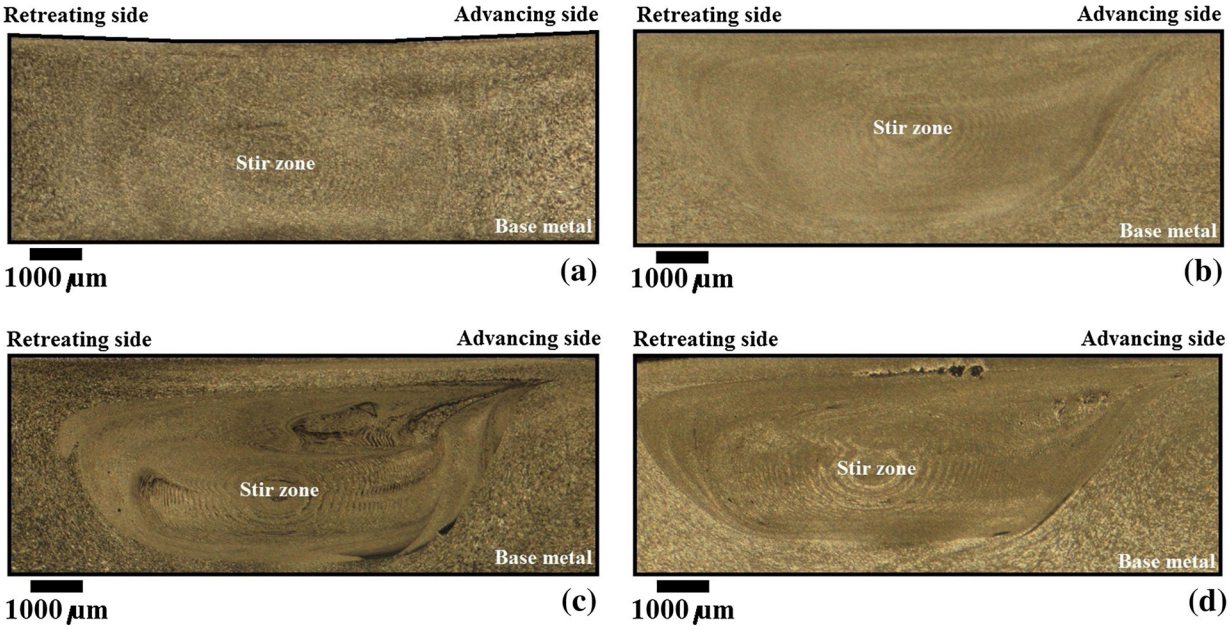

Fig. 2—Cross-sectional macroimages of friction-stir-processed sheets at (*a*) and (*c*) annealed and (*b*) and (*d*) wrought conditions. (a) and (b) Al-Mg alloy and (c) and (d) Al-Mg-TiO_2 nanocomposite.

SZ zone was seen (Figure 3). Notably, the elongated grain structure of the wrought Al-Mg alloy was changed to equiaxed. The addition of TiO_2 nanoparticles further refined the grains and caused the formation of onion ring patterns.

Microstructural evaluation of TMAZ and HAZ revealed FSP-refined grains of TMAZ with no change in HAZ structure for the annealed Al-Mg alloy and Al-Mg-TiO_2 nanocomposite (Figure 4). Notwithstanding in the specimens prepared from the wrought alloy, recrystallization of the elongated grains occurred due to the heat imposed by the rotating tool, and coarse-equiaxed grains were formed. The size of the HAZ for these samples in both advancing and retreating sides was also extended to shoulder diameter.

To further quantitatively study the grain structure of the specimens, EBSD was employed. Figure 5 shows EBSD maps of different samples. The annealed Al-Mg base alloy displayed a relatively coarse-grained structure with an average size of ~50 μm (Figure 5(a)), while the structure of the wrought alloy was elongated with a high amount of LAGBs (Figure 5(b)). FSP of the annealed Al-Mg alloy without the addition of TiO_2 nanoparticles refined the grains with sizes of about 10 μm (Figure 5(c)). The elongated structure of the wrought alloy was also diminished to form equiaxed grains with a mean size of ~6 μm (Figure 5(d)). After processing with TiO_2 nanoparticles, a finer grain structure (about 3 μm) was attained for the annealed (Figure 5(e)) and wrought (Figure 5(f)) samples. As compared to the Al-Mg alloy, the composites also contained a higher portion of LAGBs, particularly for the annealed specimen.

B. *Texture Development*

To study the effect of FSP, TiO_2 nanoparticles, and annealing on the crystallographic texture of the Al-Mg alloy, pole figures of the samples were established from the EBSD results, as shown in Figure 6. Color scales in these maps represent the intensity of different poles with the same orientation. After the FSP process, the orientation of different directions was changed due to severe plastic deformation imposed by the stirring pin and subsequent dynamic recrystallization (DRX). Hence, the intensity of crystallographic directions with the same orientation was reduced, which led to a decrease in the maximum number of the color scale after projection (compare Figures 6(e) and (f) with (a) through (d)). Analysis of the maps indicated random and rolled textures for the annealed and wrought Al-Mg alloy, respectively.

After FSP, the crystallographic texture of both sheets revealed three major textural components of Brass $\{110\}\langle 112\rangle$, Copper $\{112\}\langle 111\rangle$, and Cube $\{100\}\langle 001\rangle$. The Brass and Copper components are known to constitute a deformation texture, which is usually found in face-centered-cubic (fcc) metals.[31–34] The Cube component is a typical recrystallization texture associated with fcc metals. With the addition of TiO_2 nanoparticles and affording FSP, the severity of these texture components was improved, which can be attributed to the role of the hard (nondeformable) inclusions on the deformation flow pattern and, thereafter, DRX during FSP.[35] For the nanocomposite sample prepared from the annealed Al-Mg alloy, the Brass and Cube components were dominant, whereas the Copper

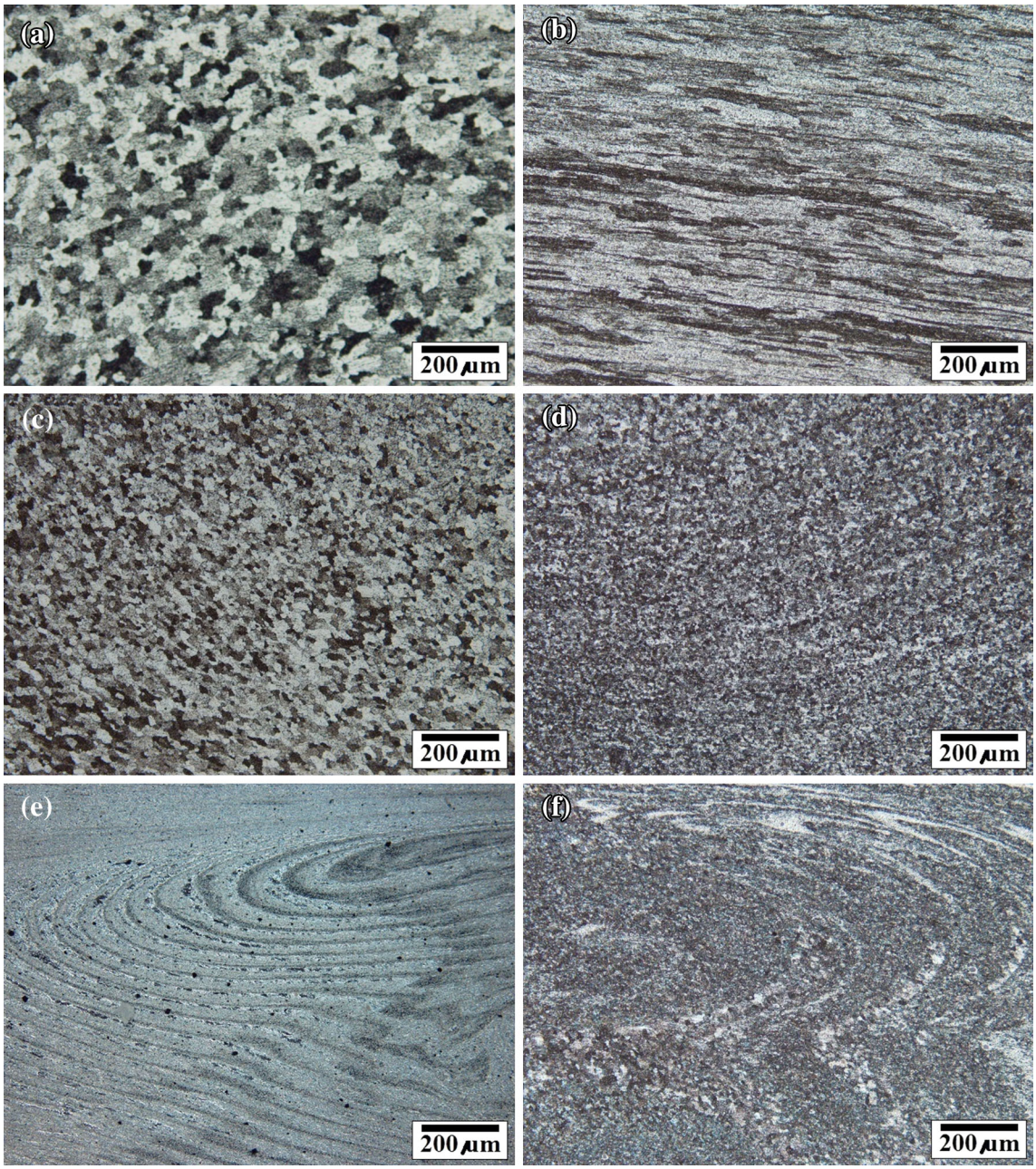

Fig. 3—Optical micrographs showing the microstructure (BM) of (*a*) annealed and (*b*) wrought Al-Mg alloy. The microstructure of the SZ of friction-stir-processed sheets: (*c*) annealed and (*d*) wrought Al-Mg alloys and (*e*) annealed and (*f*) wrought Al-Mg-TiO_2 nanocomposites.

component was relatively weak (Figure 6(e)). In contrast, the Copper component was dominant in the wrought base specimen, while the other two components were comparatively weak (Figure 6(f)).

C. *Transmission Electron Microscopy*

TEM images of the Al-Mg alloy and Al-Mg-TiO_2 nanocomposite are shown in Figure 7. The microstructure of the annealed Al-Mg alloy consisted of coarse grains, elongated (Fe, Mn, Cr)$_3$SiAl$_{12}$ precipitates, and Mg_2Si particles (Figure 7(a)). A deformed structure with a high content of subgrains and (Fe, Mn, Cr)$_3$SiAl$_{12}$ and Mg_2Si precipitates was detected in the microstructure of the wrought Al-Mg alloy (Figure 7(b)). Employing FSP caused grain refinement with a change in the morphology and size of the precipitates. Elongated rodlike Al-Fe-Mn-Si and round Mg_2Si precipitates were observed (Figures 7(c) and (d)). When TiO_2 nanoparticles were added, MgO and Al_3Ti nanoparticles were also detectable (Figures 7(e) and (f)). HRTEM studies revealed that a crystal orientation relationship $[(\bar{1}12)_{Al_3Ti}||(\bar{1}11)_{Al}]$ between the Al_3Ti particle and Al matrix existed (Figure 7(g)). The interface of MgO/Al also adopted a $(\bar{1}11)_{MgO}\perp(\bar{1}11)_{Al}$ relationship (Figure 7(h)). A coherent interface between nanosized Mg_2Si precipitates (~5 nm) and the Al matrix was seen as well (Figure 7(i)).

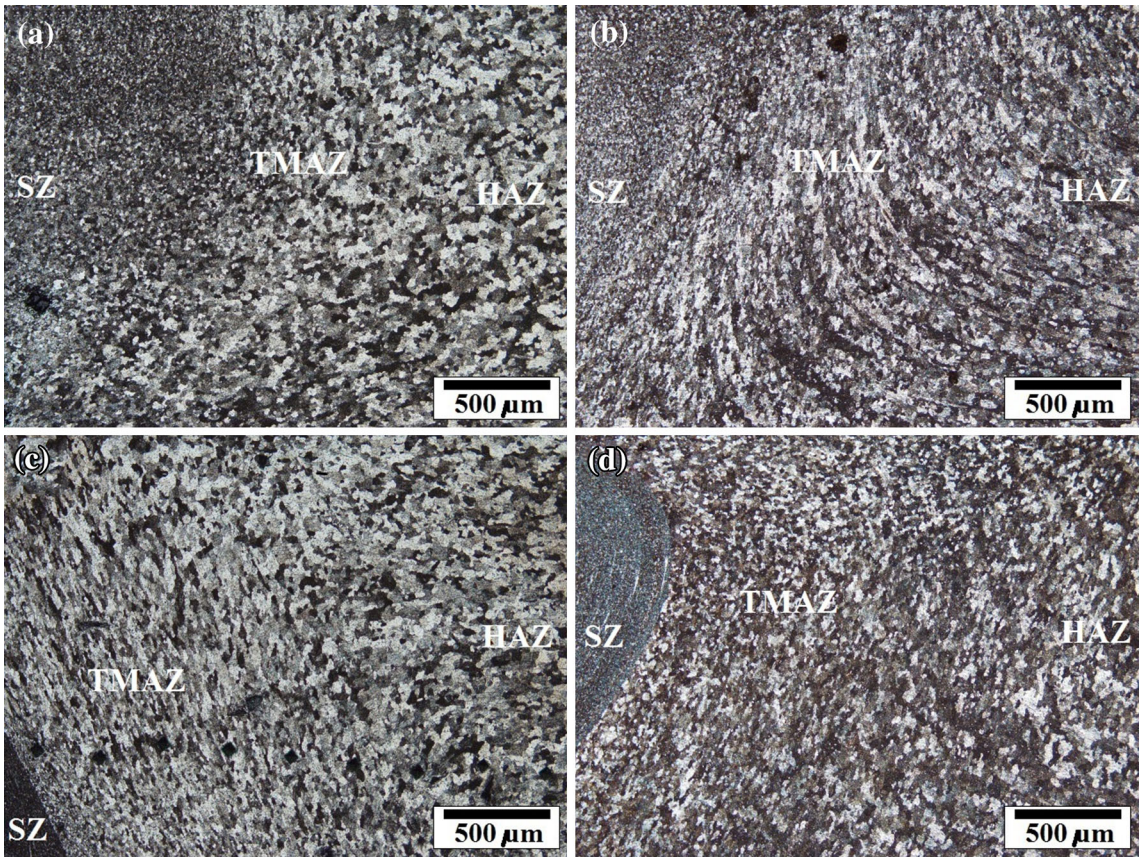

Fig. 4—Optical micrographs showing the microstructure of HAZ and TMAZ: (*a*) annealed and (*b*) wrought Al-Mg alloys and (*c*) annealed and (*d*) wrought Al-Mg-TiO_2 nanocomposites.

Table II. Average Grain Size of the Annealed and Wrought Al-Mg Alloys and Their Nanocomposites Measured at Different Zones

	Grain Size (μm)			
Sample	BM	HAZ	TMAZ	SZ
Annealed Al-Mg alloy	49.4	—	—	—
Wrought Al-Mg alloy	9.7	—	—	—
Friction-stir-processed annealed Al-Mg alloy	49.4	49.4	30.2	9.7
Friction-stir-processed wrought Al-Mg alloy	9.7	38.1	27.5	6.3
Friction-stir-processed annealed Al-Mg-TiO_2	49.4	49.4	25.3	2.9
Friction-stir-processed wrought Al-Mg-TiO_2	9.7	38.1	23.2	3.3

D. *Microhardness Profile*

Microhardness changes along different zones of the examined sheets are shown in Figure 8. The mean values of Vickers microhardness of different zones for the examined samples are reported in Table III. The results indicated that FSP improved the hardness of the SZ and TMAZ with no effect on HAZ hardness for the annealed Al-Mg alloy, notwithstanding the fact that the hardness of SZ and TMAZ reduced slightly while HAZ was softened significantly. A similar trend was seen for the nanocomposites, although higher hardness values were obtained due to the presence of reinforcement particles. Meanwhile, particle aggregation and poor material flow in the nanocomposite made from the wrought sheet yielded lower hardness values in the SZ.

E. *Tensile Testing*

Engineering stress-strain curves of the examined sheets at three strain rates are shown in Figure 9. The mechanical properties of the specimens are summarized in Table IV. The tensile flow behavior exhibited a serrated yielding phenomenon (Portevin–Le Chatelier effect) depending on the processing conditions and strain rates. A decreasing trend for the ultimate tensile strength (UTS) with the strain rate is also noticeable. To

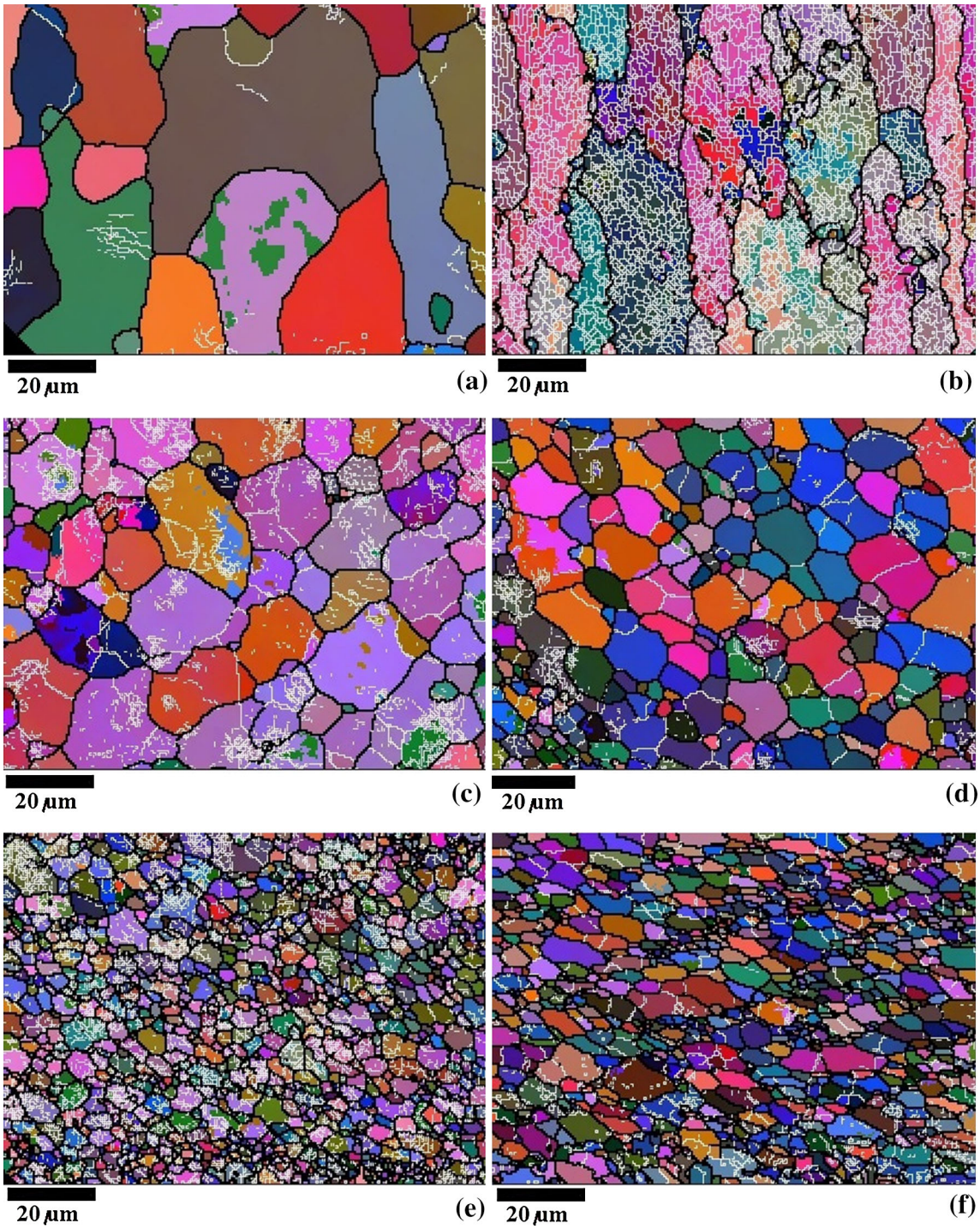

Fig. 5—EBSD maps show the grain structure of Al-Mg alloy at (*a*) annealed and (*b*) wrought conditions. EBSD maps of SZ after FSP: (*c*) annealed and (*d*) wrought Al-Mg alloys and (*e*) annealed and (*f*) wrought Al-Mg-TiO_2 nanocomposites.

evaluate the flow behavior of the materials, the strain-rate-sensitivity parameter (m) and work-hardening exponent (n) were determined by[36]

$$m = \left(\frac{\partial \ln \sigma}{\partial \ln \dot{\varepsilon}}\right) \quad [1]$$

$$n = \left(\frac{\partial \ln \sigma}{\partial \ln \varepsilon}\right) \quad [2]$$

where σ is the flow stress, ε is the strain, and $\dot{\varepsilon}$ is the strain rate. The plots of σ-$\dot{\varepsilon}$ and σ-ε in the log-log scale are shown in Figures 10(a) and (b), respectively. The

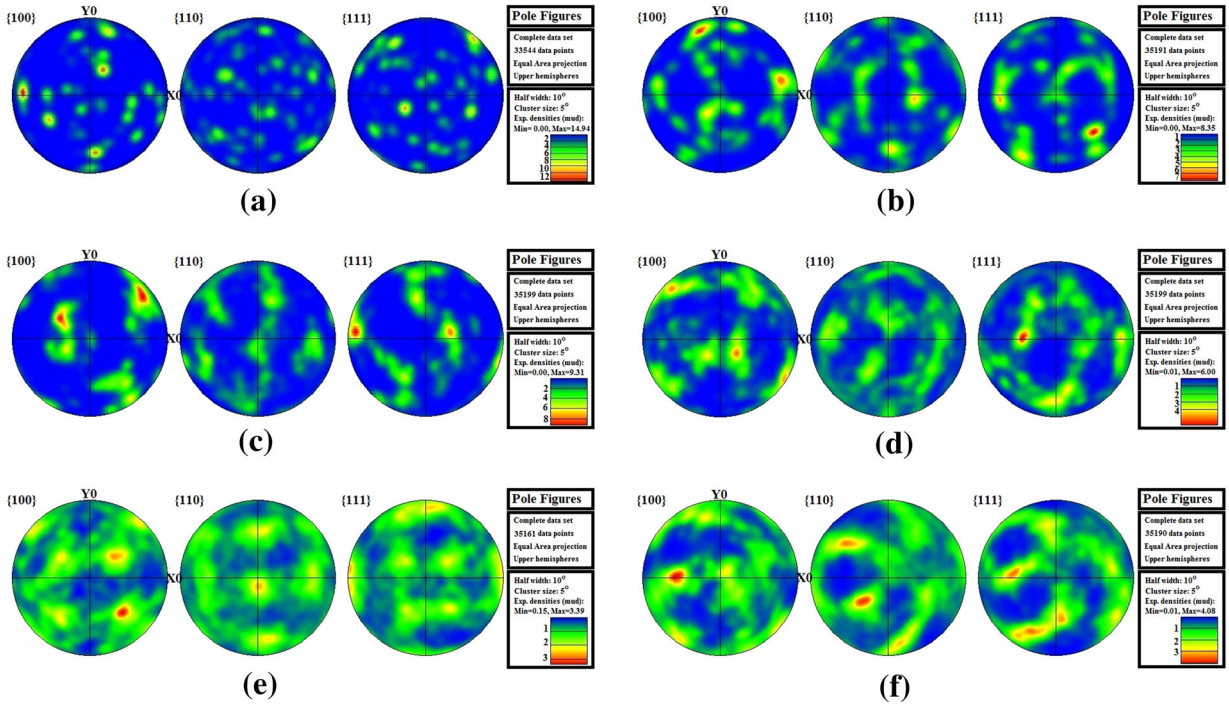

Fig. 6—Pole figures of {100}, {110}, and {111} represent textural developments in the examined materials: (*a*) annealed and (*b*) wrought Al-Mg alloys, (*c*) friction-stir-processed annealed and (*d*) wrought Al-Mg alloys, and (*e*) friction-stir-processed annealed and (*f*) wrought Al-Mg-TiO_2 nanocomposites. Note that the color scale is not the same for all maps (Color figure online).

values of *m* and *n* for different materials were calculated from the slope of the straight lines, as reported in Table IV. It appeared that FSP of the annealed Al-Mg alloy and its nanocomposite decreased strain rate sensitivity. In contrast, the *m* value of the wrought alloy and its nanocomposite increased when employing FSP. However, generally, the friction-stir-processed materials exhibited weak strain rate sensitivity. Similar results were obtained for the work-hardening exponent.

F. *Fracture Behavior*

Figures 11 and 12 show selected fracture surfaces of the tensile-tested specimens prepared from the annealed and wrought sheets at different strain rates. Characteristics of ductile fracture were observed for the annealed alloy before and after FSP without TiO_2 nanoparticles (Figures 11(a) through (c) and (e) and 12(a) through (c) and (e)). For the nanocomposites, the fracture features revealed a combined ductile-brittle rupture (Figures 11(g) and (i) and 12(g) and (i)). As the strain rate was increased, the shearlike dimples disappeared, meaning that the tensile loading component was contributed in the failure (Figures 11(a) through (c), (g), and (i) and 12(a) through (c), (g), and (i)). Additionally, with increasing the strain rate from 0.001 to 0.01 s^{-1}, the dimples became larger as an indication of more energy absorption during fracturing (Figures 11(a) and (b) and 12(a) and (b)). At a higher strain rate of 0.1 s^{-1}, a decrease in the size of dimples was noticed (Figures 11(c) and (i) and 12(c) and (i)). Similar results were obtained for the wrought alloy, but the size of dimples was finer than those of the annealed alloys (Figures 11(d) and (f) and 12(d) and (f)). This behavior was also seen for the nanocomposites, although the portion of the brittle fracture was more pronounced (Figures 11(h) and 12(h)). These failure features are related to the grain structure of the materials (Figure 5), as will be discussed in Section IV.

IV. DISCUSSION

Annealed and wrought sheets have different physical and mechanical characteristics; hence, the materials behave differently upon FSP. The prestored strain energy in the wrought sheet makes it more sensitive to the temperature rise, while the material flow is more difficult due to higher strength. Consequently, SZ becomes larger with a more intensive onion ring pattern (Figure 2). Microstructural studies also showed significant grain refinement during FSP (Figures 3 and 5), which can be related to the discontinuous dynamic recrystallization (DDRX) mechanism.[37]

Since the wrought (cold-worked) Al-Mg alloy contains a higher density of dislocations, more DDRX nuclei sites should be present, which enhance the grain refinement process (Figures 3(c) and (d) and 5(c) and (d)). On the other hand, the addition of TiO_2 nanoparticles activates other effective mechanisms on DDRX such as particle-stimulated nucleation (PSN)[38] and grain boundary pining (Zener–Holloman[39]). Consequently, the grain structure of the nanocomposites was finer than the corresponding Al-Mg alloy (Figures 3(e) and (f) and 5(e) and (f)). In addition to grain refining, new precipitates were also formed (Figure 7).

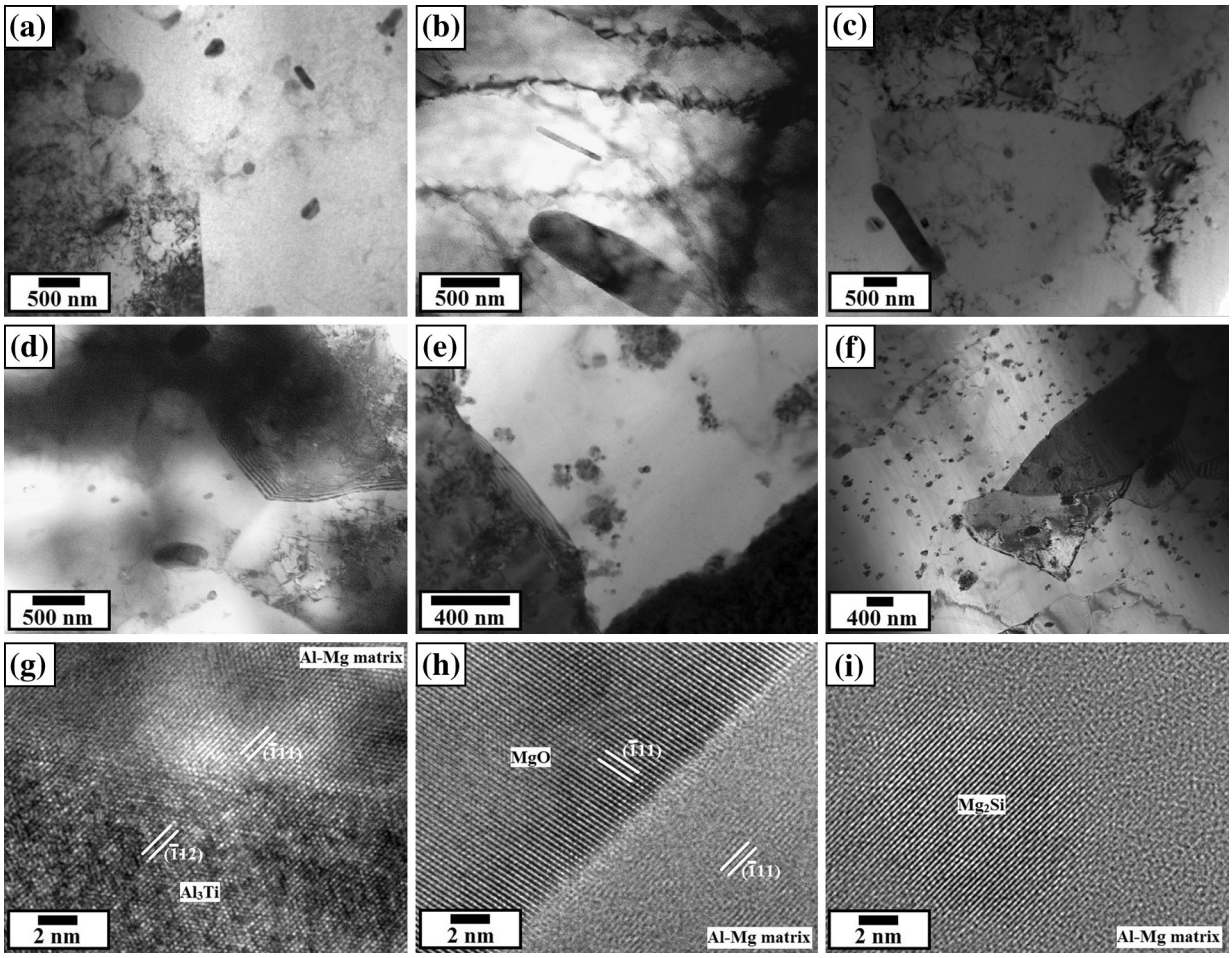

Fig. 7—TEM images of Al-Mg alloy at (*a*) annealed and (*b*) wrought conditions. The microstructure of SZ after FSP: (*c*) annealed and (*d*) wrought Al-Mg alloys and (*e*) annealed and (*f*) wrought Al-Mg-TiO_2 nanocomposites. HRTEM images show the interface of the aluminum matrix with (*g*) Al_3Ti, (*h*) MgO, and (*i*) Mg_2Si particles.

Additionally, the combination of plastic deformation and heating of the matrix modified the size and morphology of precipitates (Figures 7(c) and (d)) *via* deformation-assisted solution and reprecipitation aging mechanisms.[40]

Texture studies determined that texture components were changed by employing FSP and the addition of TiO_2 nanoparticles (Figure 6). The change in the texture components from random to a mixture of Brass, Copper, and Cube in the Al-Mg alloy could be attributed to the DRX that forms new strain-free recrystallized grains in the severely deformed zone.[41,42] The presence of hard inclusions also affected the formation of Brass/Cube and Copper textures as dominant components in the prepared nanocomposites, because hard (nondeformable) inclusions influence the flow patterns and the effectiveness of the PSN and Zener–Holloman mechanisms during DDRX.

Mechanical characterizations showed that pretreatment of the sheets and preplaced TiO_2 nanoparticles significantly affected the strength and flow behavior of the processed materials. For instance, microhardness measurement (Figure 8 and Table III) determined that grain refinement and distribution of hard inclusions during reactive FSP improved the hardness of SZ, while abnormal grain growth (Figures 3 and 4) caused hardness loss in the HAZ. Meanwhile, as the strain rate increased, the serrated flow behavior gradually disappeared (Figure 9). This behavior can be described by the effect of strain rate on the dislocation mobility and separation of dislocations from the Cottrell atmosphere.[26,43] It is well known that the deformation of crystalline alloys is controlled by the density (ρ) and mobility of dislocations (v) and, thus, by the strain rate ($\dot{\varepsilon}$) through[44]

$$\dot{\varepsilon} = \rho \mathbf{b} v \qquad [3]$$

where **b** is the Burgers vector. With increasing strain rate, the dislocation glide velocity is enhanced; hence, dislocations can detach from the locking atmosphere,

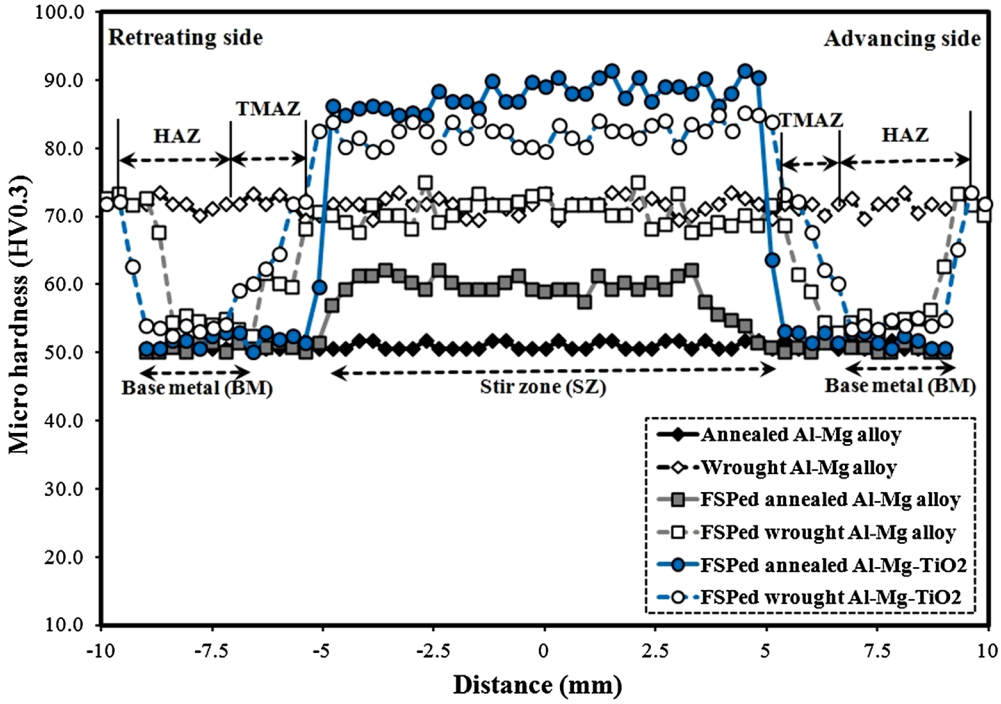

Fig. 8—Variation of Vickers microhardness along different zones of the processed materials.

Table III. Mean Values of Microhardness at Different Zones of Annealed and Wrought Al-Mg Alloys and Their Nanocomposites

	Hardness (Vickers)			
Sample	BM	HAZ	TMAZ	SZ
Annealed Al-Mg alloy	51.1 ± 0.6	—	—	—
Wrought Al-Mg alloy	71.6 ± 1.2	—	—	—
Friction-stir-processed annealed Al-Mg alloy	51.1 ± 0.6	51.1 ± 0.6	51.6 ± 0.8	59.5 ± 2.0
Friction-stir-processed wrought Al-Mg alloy	71.6 ± 1.2	55.5 ± 1.2	65.3 ± 1.7	70.8 ± 2.1
Friction-stir-processed annealed Al-Mg-TiO_2	51.1 ± 0.6	51.1 ± 0.6	61.7 ± 2.8	87.9 ± 2.0
Friction-stir-processed wrought Al-Mg-TiO_2	71.6 ± 1.2	55.4 ± 1.4	67.1 ± 0.6	82.4 ± 1.6

thus degrading the role of DSA on the flow behavior.[45] For nanocomposites, the formation of nanometric Mg_2Si precipitates and the depletion of Mg from the matrix reduce the concentration of blocking atoms, which, in fact, affects the serrated flow behavior with respect to the BM and friction-stir-processed Al-Mg alloys.

Tensile testing at different strain rates exhibited the effect of pretreatment and TiO_2 nanoparticles on the strain rate sensitivity and work-hardening behavior (Figure 10). The relationship between the flow stress (σ) and strain rate can be expressed as[44]

$$\sigma = \left(\frac{1}{\rho b v_0 \Omega(\sigma)} \exp\left[\frac{\Delta G(\sigma)}{kT}\right]\right)^m (\dot{\varepsilon})^m, \qquad [4]$$

where $\Delta G(\sigma)$ is the activation energy, $\Omega(\sigma)$ is the average distance traveled by the dislocation segment, v_0 is frequency, k is the Boltzmann constant, and T is temperature. Equation [4] indicates that a lower dislocation density enhances the flow stress. Since DDRX is strongly operative during FSP of the wrought Al-Mg alloy (as evidenced from the microstructure), it is expected that the density of dislocations is reduced. Consequently, increasing the strain rate enhanced the yield stress. On the other hand, the presence of nonshearable and nanometric inclusions in the nanocomposite impacts the dislocation density *via* thermal mismatch with the metal matrix and Orowan mechanism. Therefore, a positive dependent of the yield stress to strain rate, *i.e.*, higher m value, was attained.

Fractographic studies indicated different fracture aspects of ductile and brittle models depending on the strain rate, grain structure, and processing condition (Figures 11 and 12). It was shown that the annealed, wrought, and friction-stir-processed Al-Mg alloys exhibited a typical ductile fracture with deep equiaxed dimples (Figures 11(a) through (c) and (e) and 12(a) through (c) and (e)). A large amount of deformation and necking was also observed. Ductile fracture in most materials has a gray fibrous appearance with equiaxed or hemispheroidal dimples.[46,47] This kind of fracture occurs by the nucleation of

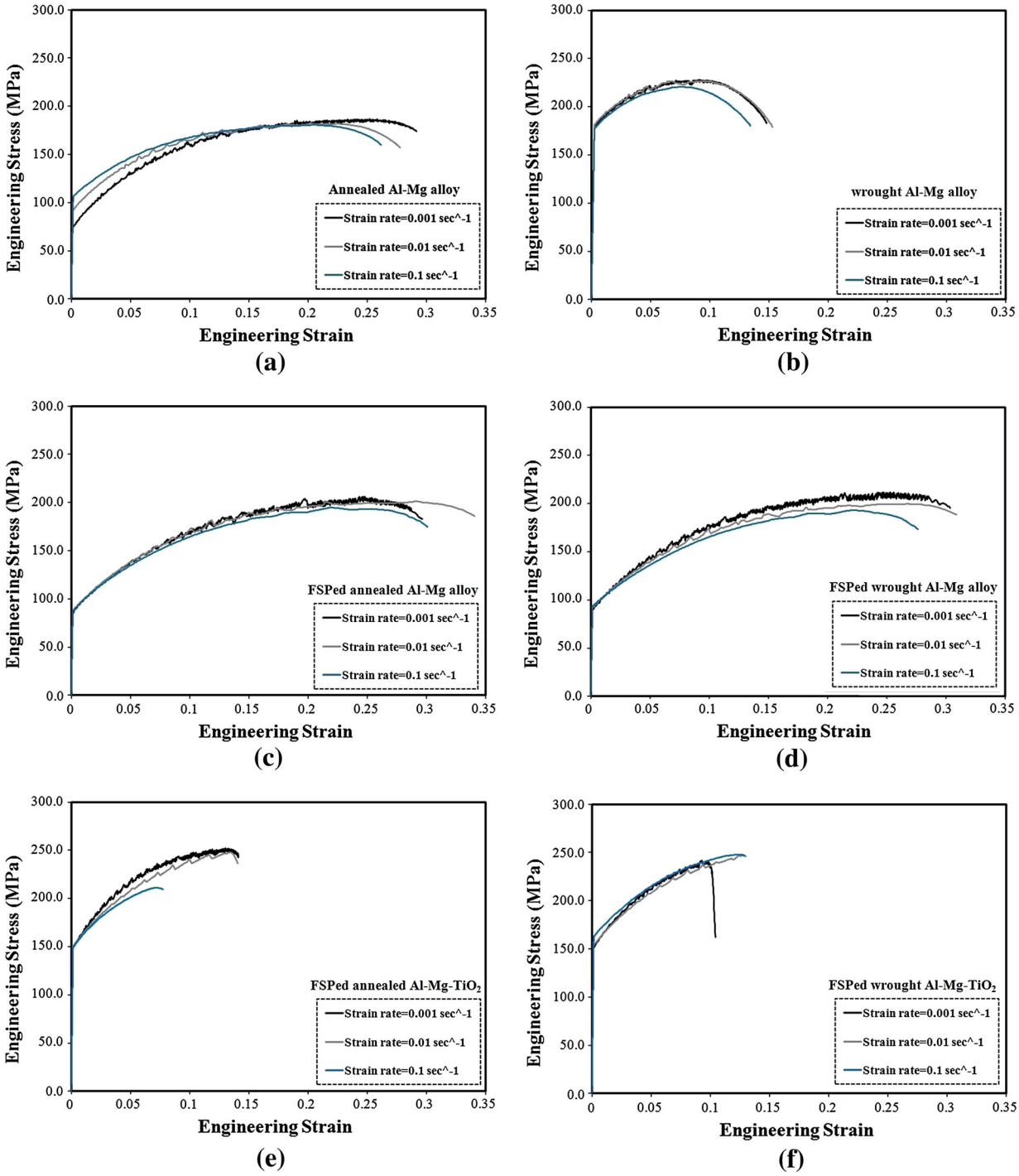

Fig. 9—Effect of strain rate on the engineering stress-strain curves of Al-Mg sheets and their nanocomposites: (*a*) annealed and (*b*) wrought Al-Mg alloys; friction-stir-processed (*c*) annealed and (*d*) wrought Al-Mg alloys; and (*e*) annealed and (*f*) wrought Al-Mg-TiO_2 nanocomposites at strain rates of 0.001, 0.01, and 0.1 s^{-1}.

microvoids followed by their growth and coalescence depending on the state of stresses. When failure is controlled by a shear stress, elongated voids and dimples with parabolic depressions are observed. A change in the morphology of dimples from parabolic equiaxed to hemispherical at higher strain rates (Figures 11(a) through (c) and 12(a) through (c)) indicates that tensile fracture became dominant as compared to shear rupture.[47] In other words, rapid loading can retard shear banding while fracture proceeds under tensile condition. Consequently, the failure that occurs is less ductile with small dimple features.

Table IV. Effect of Pretreatment, FSP, and Strain Rate on the Tensile Properties of Al-Mg Alloy and Al-Mg-TiO_2 Nanocomposite

Property	Processing	σ_y* (MPa)			σ_{UTS}** (MPa)			σ_f† (MPa)			$e^{\ddagger}$ (Pct)				
Strain rate, s^{-1}		10^{-3}	10^{-2}	10^{-1}	10^{-3}	10^{-2}	10^{-1}	10^{-3}	10^{-2}	10^{-1}	10^{-3}	10^{-2}	10^{-1}	m	n
Al-Mg alloy	annealed	74	92	107	186	182	180	176	160	162	29.2	27.8	26.2	0.185	0.335
	wrought	178	183	180	227	226	220	183	183	183	14.8	15.3	13.4	0.006	0.119
	annealed/FSP	86	88	88	206	201	195	183	186	174	29.6	34.1	30.1	0.016	0.330
	wrought/FSP	89	92	94	211	200	193	195	188	174	30.4	30.9	27.6	0.025	0.326
Al-Mg-TiO_2	annealed/FSP	148	151	149	252	248	211	242	239	211	14.1	14.0	7.7	0.003	0.204
	wrought/FSP	151	154	163	240	254	248	162	247	248	10.4	12.8	12.9	0.037	0.184

*Yield strength.
**Ultimate tensile strength.
†Fracture stress.
‡Elongation at fracture.

Although the ductile fracture mode was observed in the fracture surfaces of friction-stir-processed specimens, the dimples were not as deep as those in the base Al-Mg alloys (Figures 11(d) and (f) and 12(d) and (f)). For nanocomposites, the hard inclusions can serve as preferential sites for microvoid nucleation due to decohesion of the particles from the matrix and also inhibit crack growth by deflection.[46] As a result, finer dimples were formed (Figures 11(g) through (i) and 12(g) through (i)). A relationship between the dimple sizes with the grain structure of the Al-Mg alloy without TiO_2 nanoparticles (Figure 5 and Table II) was also noticed. Since grain boundaries affect nucleation and propagation of microvoids,[48] the fracture surfaces of those samples with finer grain structure should exhibit shallower dimples during tensile failure (Figures 11(a) through (f) and 12(a) through (f)). However, in the presence of hard inclusions, the formation of microvoids is strongly controlled by the detachment of the particles from the matrix; thereby, the vital role of grain boundaries is diminished and the size of dimples becomes finer compared to that of unreinforced specimens.

V. CONCLUSIONS

Al-2.2 pct Mg-3 vol pct TiO_2 nanocomposite was fabricated by FSP. The effect of sheet pretreatment (annealing or cold working) on the microstructural evolution, texture development, and fracture behavior was studied. The flow behavior of the materials at different strain rates was investigated by determining the strain-rate-sensitivity parameter (m) and work-hardening exponent (n). The main conclusions can be summarized as follows.

1. Larger SZ size, less homogenous particle flow, sharper onion ring pattern, and finer grain structure with more HAGB content were attained for the wrought Al-Mg alloy and its nanocomposite.
2. Comparison of the pole figures revealed that the initial random and rolling preferred crystallographic orientations for the annealed and wrought Al-Mg alloys were modified to a mixture texture component of Brass, Copper, and Cube after FSP. Brass/Cube and Copper crystallographic textures were detected as dominant components for the nanocomposites prepared from the annealed and wrought sheets, respectively.
3. Al_3Ti and MgO nanoparticles were formed *in situ* during FSP as a result of solid-state reactions between Al-Mg base alloy and TiO_2 nanoparticles.
4. Analysis of the flow behavior of the examined materials revealed that annealing of the wrought sheets decreased the strain rate sensitivity and work hardening of the Al-Mg alloy. Similarly,

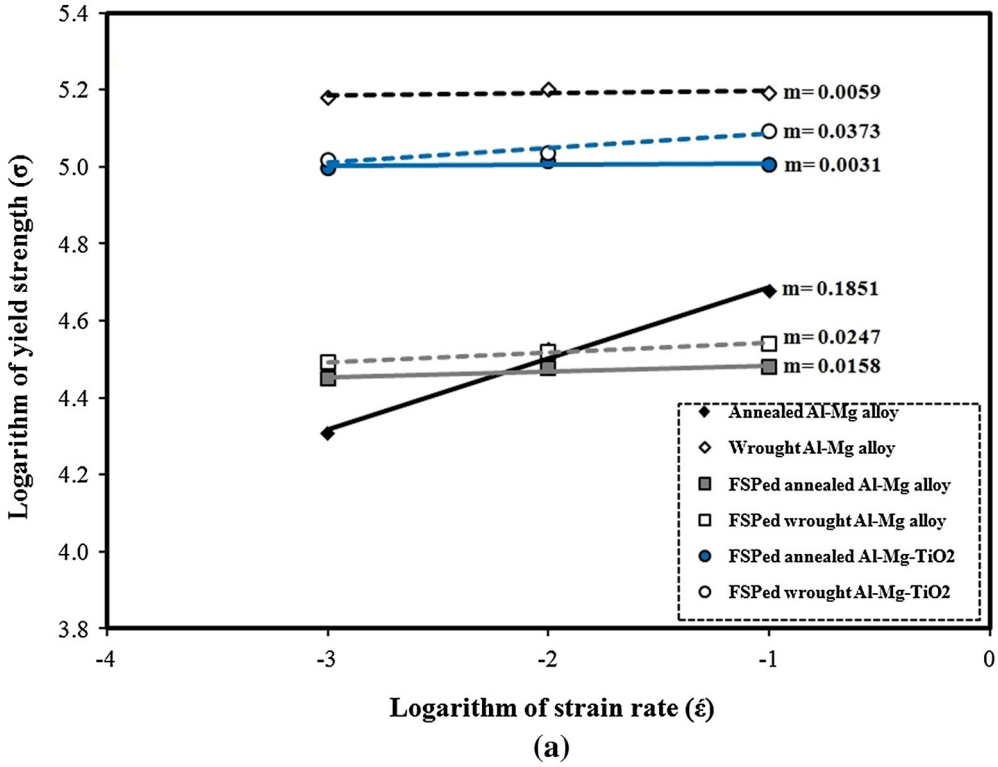

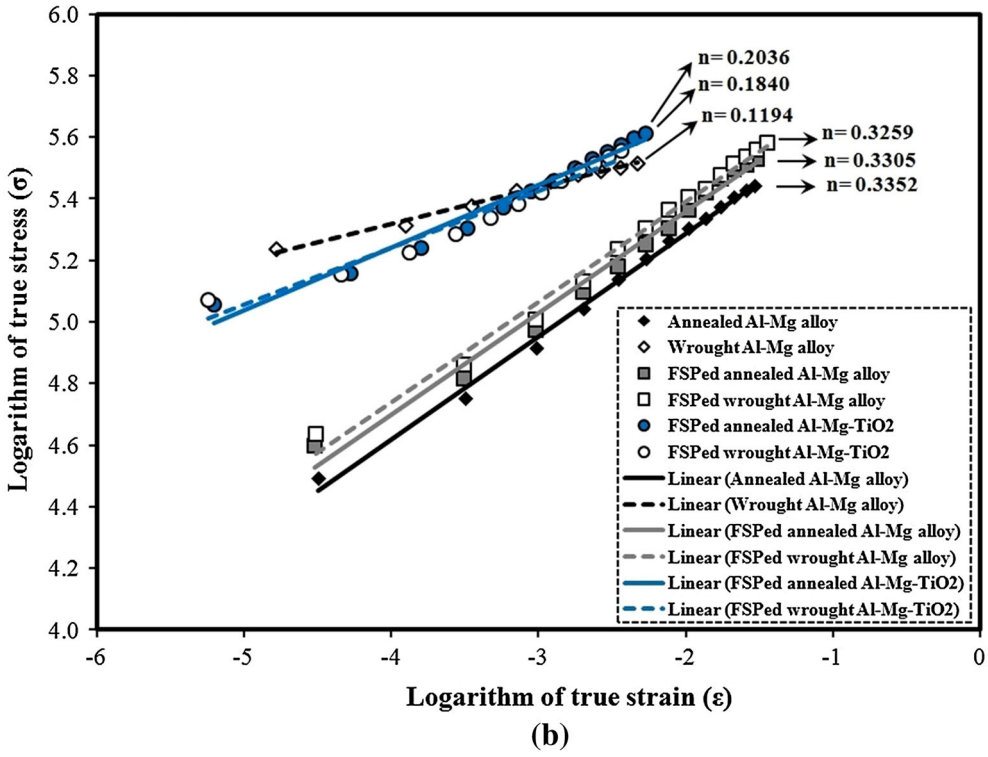

Fig. 10—Plots of (*a*) σ-$\dot{\varepsilon}$ and (*b*) σ-ε for the examined sheets. The slope of the straight lines yields values of the strain-rate-sensitivity parameter (m) and work-hardening exponent (n).

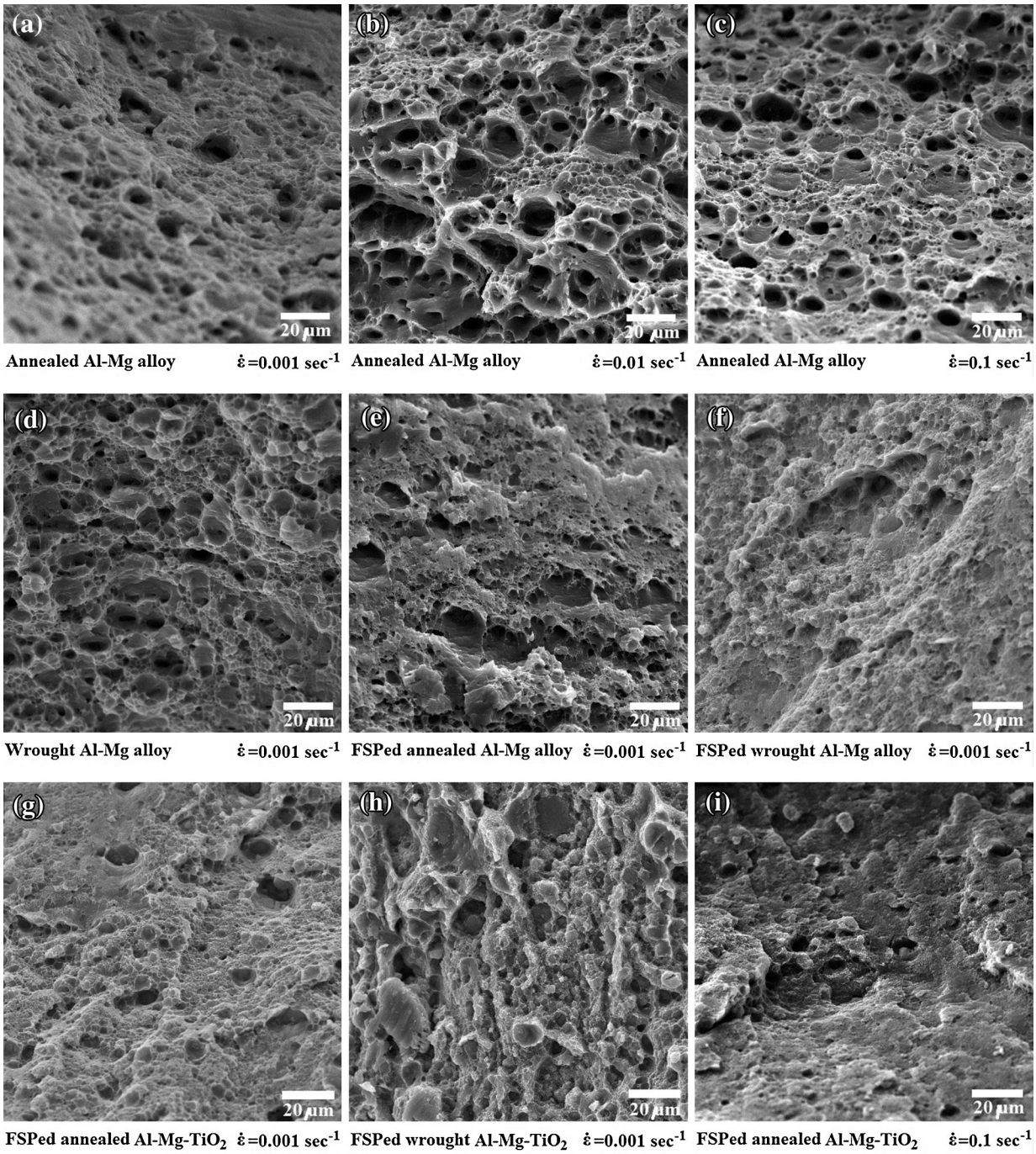

Fig. 11—FESEM images show the tensile fracture surfaces of (*a*) through (*f*) Al-Mg sheets and (*g*) through (*i*) Al-Mg-TiO_2 nanocomposites tested at different strain rates. Annealed Al-Mg alloy at (a) $\dot{\varepsilon} = 0.001\ s^{-1}$, (b) $\dot{\varepsilon} = 0.001\ s^{-1}$, and (c) $\dot{\varepsilon} = 0.1\ s^{-1}$; (d) wrought Al-Mg alloy at $\dot{\varepsilon} = 0.001\ s^{-1}$; (e) friction-stir-processed annealed Al-Mg alloy at $\dot{\varepsilon} = 0.001\ s^{-1}$; (f) friction-stir-processed wrought Al-Mg alloy at $\dot{\varepsilon} = 0.001\ s^{-1}$; Al-Mg-$TiO_2$ nanocomposite from annealed base at (g) $\dot{\varepsilon} = 0.001\ s^{-1}$ and (i) $0.1\ s^{-1}$; and (h) Al-Mg-TiO_2 nanocomposite from wrought base at $\dot{\varepsilon} = 0.001\ s^{-1}$ (×1000 magnification).

the addition of TiO_2 nanoparticles and formation of Al_3Ti and MgO inclusions reduced the values of *m* and *n*.

5. Failure of the friction-stir-processed nanocomposites was performed in a ductile-brittle mode, while the unreinforced alloy exhibited ductile rupture behavior. At higher strain rates, the fracture mechanism was changed from shear to tensile failure, which was detectable by formation of microscopic finer hemispherical equiaxed dimples.

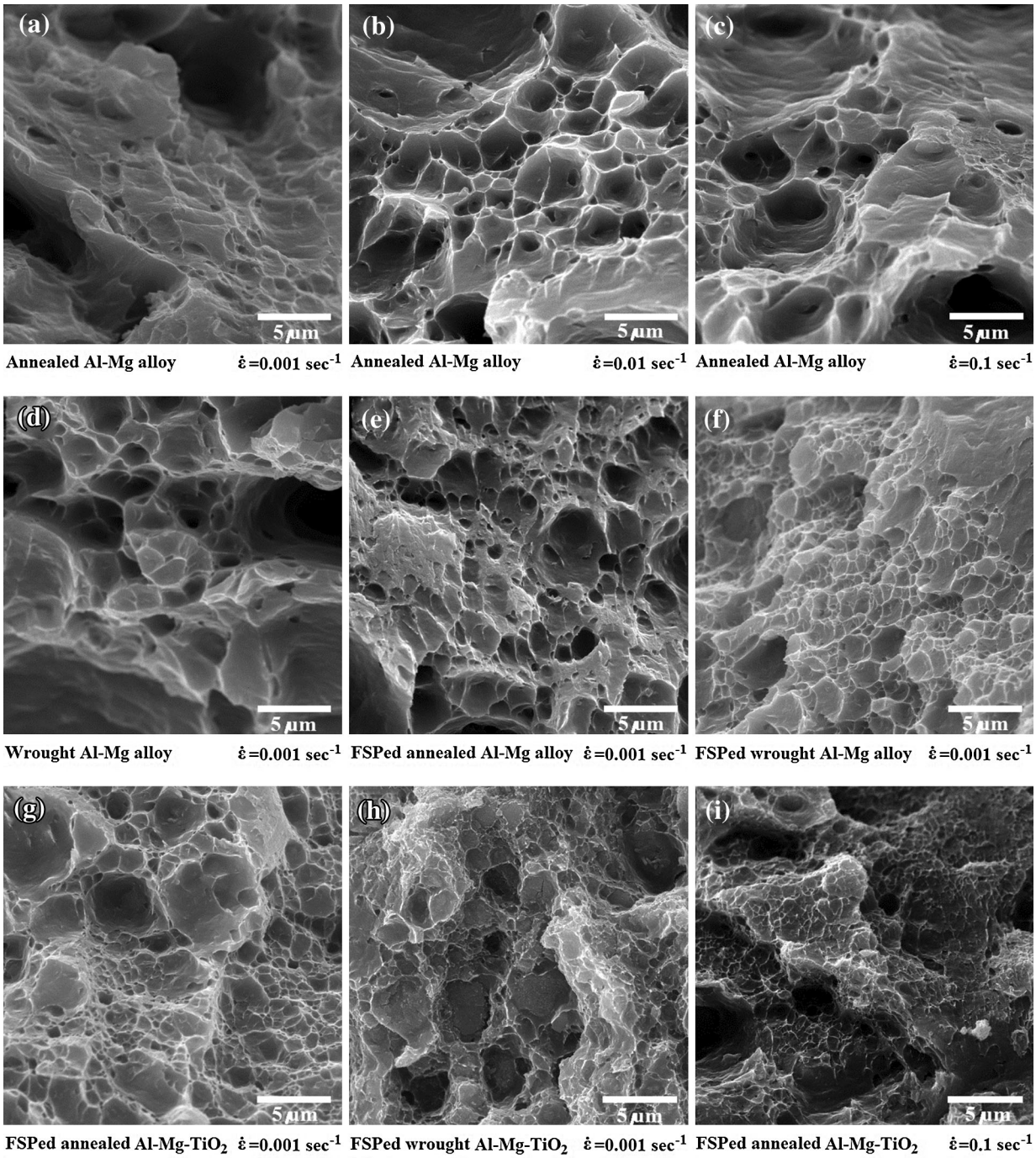

Fig. 12—FESEM images show the tensile fracture surfaces of (*a*) through (*f*) Al-Mg sheets and (*g*) through (*i*) Al-Mg-TiO_2 nanocomposites tested at different strain rates. Annealed Al-Mg alloy at (a) $\dot{\varepsilon} = 0.001\ s^{-1}$, (b) $\dot{\varepsilon} = 0.001\ s^{-1}$, and (c) $\dot{\varepsilon} = 0.001\ s^{-1}$; (d) wrought Al-Mg alloy at $\dot{\varepsilon} = 0.001\ s^{-1}$; (e) friction-stir-processed annealed Al-Mg alloy at $\dot{\varepsilon} = 0.001\ s^{-1}$; (f) friction-stir-processed wrought Al-Mg alloy at $\dot{\varepsilon} = 0.001\ s^{-1}$; Al-Mg-$TiO_2$ nanocomposite prepared from the annealed alloy at (g) $\dot{\varepsilon} = 0.001\ s^{-1}$ and (i) $0.1\ s^{-1}$; and (h) Al-Mg-TiO_2 nanocomposite prepared from the wrought alloy at $\dot{\varepsilon} = 0.001\ s^{-1}$ (×6000 magnification).

ACKNOWLEDGMENT

The authors thank Dr. Frantisek Simančík, Institute of Materials and Machine Mechanics, Slovak Academy of Sciences, for useful discussions and help in performing the experiments.

REFERENCES

1. T.W. Clyne and P.J. Withers: *An Introduction to Metal Matrix Composites*, Cambridge University Press, Cambridge, 1993.
2. T.S. Srivatsan, T.S. Sudarshan, and E.J. Lavernia: *Prog. Mater Sci.*, 1995, vol. 39, pp. 317–409.
3. C. Suryanarayana: *J. Alloys Compd.*, 2011, vol. 509, pp. 229–34.

4. C. Suryanarayana and N. Al-Aqeeli: *Prog. Mater Sci.*, 2013, vol. 58, pp. 383–502.
5. H. Asgharzadeh, A. Simchi, and H.S. Kim: *Mater. Sci. Eng. A*, 2010, vol. 527, pp. 4897–4905.
6. M. Krasnowski and T. Kulik: *Scripta Mater.*, 2003, vol. 48, pp. 1489–94.
7. H.X. Peng, D.Z. Wang, L. Geng, C.K. Yao, and J.F. Mao: *Scripta Mater.*, 1997, vol. 37, pp. 199–204.
8. H. Nasiri, J. Vahdati Khaki, and S.M. Zebarjad: *J. Alloys Compd.*, 2011, vol. 509, pp. 5305–08.
9. B. Adamczyk-Cieślak, J. Mizera, and K.J. Kurzydłowski: *Mater. Charact.*, 2011, vol. 62, pp. 327–32.
10. C.J. Hsu, C.Y. Chang, P.W. Kao, N.J. Ho, and C.P. Chang: *Acta Mater.*, 2006, vol. 54, pp. 5241–49.
11. C.J. Hsu, P.W. Kao, and N.J. Ho: *Scripta Mater.*, 2005, vol. 53, pp. 341–45.
12. I.S. Lee, P.W. Kao, and N.J. Ho: *Intermetallics*, 2008, vol. 16, pp. 1104–08.
13. Q. Liu, L. Ke, F. Liu, C. Huang, and L. Xing: *Mater. Des.*, 2013, vol. 45, pp. 343–48.
14. M.A. Moghaddas and S.F. Kashani-Bozorg: *Mater. Sci. Eng. A*, 2013, vol. 559, pp. 187–93.
15. J. Qian, J. Li, J. Xiong, F. Zhang, and X. Lin: *Mater. Sci. Eng. A*, 2012, vol. 550, pp. 279–85.
16. M. Yang, C. Xu, C. Wu, K.C. Lin, Y.J. Chao, and L. An: *J. Mater. Sci.*, 2010, vol. 45, pp. 4431–38.
17. Q. Zhang, B.L. Xiao, W.G. Wang, and Z.Y. Ma: *Acta Mater.*, 2012, vol. 60, pp. 7090–7103.
18. R.S. Mishra, Z.Y. Ma, and I. Charit: *Mater. Sci. Eng. A*, 2003, vol. 341, pp. 307–10.
19. Q. Zhang, B.L. Xiao, D. Wang, and Z.Y. Ma: *Mater. Chem. Phys.*, 2011, vol. 130, pp. 1109–17.
20. Q. Zhang, B.L. Xiao, Q.Z. Wang, and Z.Y. Ma: *Mater. Lett.*, 2011, vol. 65, pp. 2070–72.
21. L. Ke, C. Huang, L. Xing, and K. Huang: *J. Alloys Compd.*, 2010, vol. 503, pp. 494–99.
22. X. Feng, H. Liu, and S. Suresh Babu: *Scripta Mater.*, 2011, vol. 65, pp. 1057–60.
23. F. Iida, T. Suzuki, E. Kuramoto, and S. Takeuchi: *Acta Metall.*, 1979, vol. 27, pp. 637–47.
24. R. Korla and A.H. Chokshi: *Scripta Mater.*, 2010, vol. 63, pp. 913–16.
25. F. Li: *Scripta Metall. Mater.*, 1995, vol. 32, pp. 463–68.
26. A.C. Magee and L. Ladani: *Mater. Sci. Eng. A*, 2013, vol. 582, pp. 276–83.
27. E. Romhanji, M. Dudukovska, and D. Glišić: *J. Mater. Process. Technol.*, 2002, vols. 125–126, pp. 193–98.
28. K.C. Chan and G.Q. Tong: *Mater. Lett.*, 2001, vol. 51, pp. 389–95.
29. M.O. Lai, L. Lu, and B.Y. Chung: *Compos. Struct.*, 2002, vol. 57, pp. 183–187.
30. ASTM Standard E8M: *Tension Testing of Metallic Materials*, Annual Book of ASTM Standards, ASTM, West Conshohocken, PA, 1998.
31. M.M.Z. Ahmed, B.P. Wynne, W.M. Rainforth, and P.L. Threadgill: *Scripta Mater.*, 2011, vol. 64, pp. 45–48.
32. M.M.Z. Ahmed, B.P. Wynne, W.M. Rainforth, and P.L. Threadgill: *Mater. Charact.*, 2012, vol. 64, pp. 107–17.
33. U.F.H.R. Suhuddin, S. Mironov, Y.S. Sato, and H. Kokawa: *Mater. Sci. Eng. A*, 2010, vol. 527, pp. 1962–69.
34. S. Mironov, K. Masaki, Y.S. Sato, and H. Kokawa: *Metall. Mater. Trans. A*, 2013, vol. 44A, pp. 1153–57.
35. W.F. Hosford: *The Mechanics of Crystals and Textured Polycrystals*, 3rd ed., Oxford University Press, New York, NY, 1993.
36. K.K. Chawla and M.A. Meyers: in *Encyclopedia of Physical Science and Technology* (Third Edition), Robert A. Meyers, ed., Academic Press, New York, NY, 2003, pp. 467–84.
37. T.R. McNelley, S. Swaminathan, and J.Q. Su: *Scripta Mater.*, 2008, vol. 58, pp. 349–54.
38. L.P. Troeger and E.A. Starke, Jr: *Mater. Sci. Eng. A*, 2000, vol. 293, pp. 19–29.
39. C.I. Chang, C.J. Lee, and J.C. Huang: *Scripta Mater.*, 2004, vol. 51, pp. 509–14.
40. W. Woo, H. Choo, D.W. Brown, S.C. Vogel, P.K. Liaw, and Z. Feng: *Acta Mater.*, 2006, vol. 54, pp. 3871–82.
41. T. Shibayanagi, A.P. Gerlich, K. Kashihara, and T.H. North: *Metall. Mater. Trans. A*, 2009, vol. 40A, pp. 920–31.
42. D.P. Field, T.W. Nelson, Y. Hovanski, and K.V. Jata: *Metall. Mater. Trans. A*, 2001, vol. 32A, pp. 2869–77.
43. E.O. Hall: *Yield Point Phenomena in Metals and Alloys*, Plenum Press, New York, NY, 1970.
44. Y. Huang, W. Zheng, and J. Shen: *Metall. Mater. Trans. A*, 2012, vol. 43A, pp. 5202–08.
45. S. Ig Hong: *Mater. Sci. Eng.*, 1986, vol. 82, pp. 175–85.
46. V.A. Romanova, R.R. Balokhonov, and S. Schmauder: *Acta Mater.*, 2009, vol. 57, pp. 97–107.
47. V.M. Segal: *Mater. Sci. Eng. A*, 2005, vol. 406, pp. 205–16.
48. K. Manigandan, T.S. Srivatsan, D. Tammana, B. Poorganji, and V.K. Vasudevan: *Mater. Sci. Eng. A*, 2014, vol. 601, pp. 29–39.